TTMP vol 2 (3), 2025
doi: 10.30511/TTMP.2025.2064964.1056

Transactions in Theoretical and Mathematical Physics

Numerical Study of a Nanoscale Waveguide with Brillouin Scattering

Maryam Zoghi *

School of Engineering Science, College of Engineering, 16 Azar Street, Tehran, Iran

Received: 07 July 2025 / Accepted: 09 July 2025 / Published: 09 July 2025

Abstract Stimulated Brillouin scattering (SBS) arises from the interaction between light and sound waves. In partially suspended waveguides, reduced substrate contact enhances optical and acoustic confinement, improving SBS efficiency. This study uses two-dimensional finite element simulations to analyze SBS in a silicon waveguide anchored by a silica pillar. Both forward and backward SBS are explored across a broad frequency range. Optimizing the pillar width significantly increases SBS gain, mainly through the photoelastic effect, with minor moving boundary contributions. The results emphasize the importance of structural design in enhancing SBS for high-performance integrated photonic applications.

1 Introduction

Stimulated Brillouin scattering (SBS) is a nonlinear phenomenon in which light coherently interacts with acoustic vibrations within an optically transparent medium [1]. This process was predicted by Brillouin in 1922 [2] and was first experimentally verified shortly after the advent of the laser [3]. While SBS was initially regarded as a detrimental effect in optical fiber systems [4], its applications are increasingly recognized in narrow line-width lasers [5,6], microwave photonics filters [7,8], non-reciprocal components [9,10], light storage [11,12], and optical gyroscopes [13]. At elevated optical intensities, the interference pattern formed between two optical waves (referred to as the 'pump' and the 'Stokes seed', which are initially induced by thermal phonons) produces sound, which in turn creates a travelling index grating that scatters light. This phenomenon induces a back-action drive of the mechanical waves through electrostriction and radiation pressure forces [1]. Such feedback results in the so-called backward Stimulated Brillouin Scattering (SBS) effect (Fig. 1).

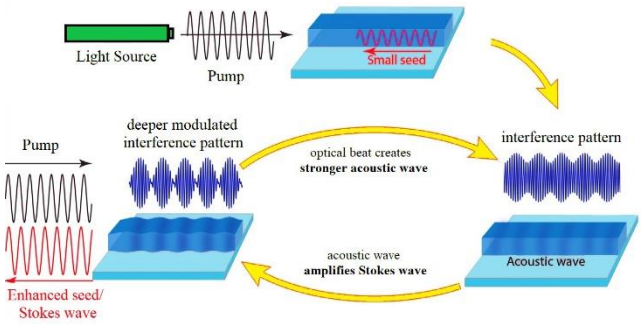

Fig. 1 Stimulated Brillouin scattering.

Over the past decade, thanks to the development and accessibility of sophisticated top-down nanofabrication tools, significant research advances have been made in this field, both in classical [14] and quantum [15] contexts. The progress made on these integrated-photonic structures led to a merging of traditional waveguide-based Brillouin concepts with those of cavity optomechanics. A notable result of this integration was the prediction and later demonstration of Brillouin scattering with giant gain in a Complementary Metal-Oxide-Semiconductor (CMOS)-compatible platform [16]. The suspended rectangular silicon waveguide structure exemplifies a particular kind of waveguide design that is preferred in the field of nanophotonics due to its ability to provide optical confinement and enable low-loss propagation. In this research, we investigate SBS within a rectangular suspended waveguide composed of silicon on an etched silica substrate using numerical modelling.

2 Physics of Brillouin Scattering

* e-mail: maryam.zoghi@ut.ac.ir

Given that the refractive index of the waveguide exceeds that of the surrounding material, this configuration will facilitate confined optical modes characterized by a specific angular frequency ω and wave number k. The determination of these modes, along with their corresponding modal fields, can be achieved through various numerical techniques, all of which address Maxwell's equations on the cross-section while applying suitable boundary conditions at the periphery of the computational domain.

2.1 Optical Mode Equations

We begin with Maxwell's equations:

$$\boldsymbol{\nabla} \times \boldsymbol{E} = -\partial_t \boldsymbol{B}, \tag{1}$$

$$\boldsymbol{\nabla} \times \boldsymbol{H} = \partial_t \boldsymbol{D} + \boldsymbol{J}, \tag{2}$$

where $\boldsymbol{D}$ and $\boldsymbol{B}$ are the electric and magnetic induction fields, respectively; $\boldsymbol{E}$ and $\boldsymbol{H}$ denote the electric and magnetic fields, respectively; $\boldsymbol{J}$ signifies the dissipative current resulting from ohmic losses, and $\boldsymbol{\nabla}$ indicates the three-dimensional del operator. The symbol ∂_t represents the partial derivative with respect to time. By introducing the constitutive expansions $\boldsymbol{B} = \mu \boldsymbol{H}$, $\boldsymbol{D} = \varepsilon \boldsymbol{E} + \boldsymbol{P}^{NL}$, and $\boldsymbol{J} = \sigma \boldsymbol{E}$, and $\boldsymbol{P}^{NL} (= \Delta\varepsilon\, \boldsymbol{E}$, assuming no nonlinear magnetic effects, with $\Delta\varepsilon$ as the perturbation), signifies the nonlinear polarization field, and $\varepsilon (= \varepsilon^R - i\sigma\omega)$, σ, and μ denote the permittivity, ohmic conductance, and permeability of the medium, respectively. If we define $|\Psi\rangle = \binom{\boldsymbol{E}}{\boldsymbol{H}}$, with the expansion as

$$|\Psi(x,y,z,t)\rangle = a_n \exp i(k_n z - \omega_n t)\, |\Psi_n(x,y)\rangle + c.c. \tag{3}$$

The transverse optical modes can then be derived from vector Helmholtz equation [17]:

$$(\mathbb{D}^{op} + i k_n \mathbb{P}^{op})|\Psi_n\rangle = i\, \omega_n\, \mathbb{E}^{op}\, |\Psi_n\rangle. \tag{4}$$

With

$$\mathbb{E}^{op} = \begin{pmatrix} \varepsilon^R & 0 \\ 0 & \mu \end{pmatrix}, \tag{5.a}$$

$$\Delta\mathbb{E}^{op} = \begin{pmatrix} \Delta\varepsilon & 0 \\ 0 & 0 \end{pmatrix}, \tag{5.b}$$

$$\mathbb{P}^{op} = \begin{pmatrix} 0 & -\hat{\boldsymbol{z}} \times \\ \hat{\boldsymbol{z}} \times & \mu \end{pmatrix}, \tag{5.c}$$

$$\mathbb{D}^{op} = \begin{pmatrix} 0 & -\boldsymbol{\nabla}_\perp \times \\ \boldsymbol{\nabla}_\perp \times & 0 \end{pmatrix}, \tag{5.d}$$

where $\boldsymbol{\nabla} = \boldsymbol{\nabla}_\perp + \hat{\boldsymbol{z}}\, \partial_z$ and $\hat{\boldsymbol{z}} = (0,0,1)$.

2.2 Acoustic Mode Equation

The mechanical counterpart to Maxwell's equations is represented by the equations of linear elasticity, which encompass the relationship between strain and mechanical displacement, as well as the principle of momentum conservation. Assuming that the acoustic losses are weak, we have:

$$\boldsymbol{S} = \nabla_s \mathbf{U}, \tag{6}$$

$$\rho\, \partial_t^2 \mathbf{U} = \boldsymbol{\nabla}.\mathbf{T}\,, \tag{7}$$

where $\boldsymbol{S}$ represents the linear strain tensor, ∇_s signifies the symmetric gradient operator, $\mathbf{U}$ denotes the infinitesimal mechanical displacement vector, ρ indicates the mass density, and $\mathbf{T}$ refers to the stress tensor (Cauchy stress), which in the absence of loss assumes the following form

$$\mathrm{T}_{ij} = c_{ijkl}\, S_{kl}\,, \quad \text{or} \quad \boldsymbol{T} = \boldsymbol{c}\!:\!\boldsymbol{S}\,. \tag{8}$$

In this context, we define the fourth-rank sffness tensor c_{ijkl} that characterizes the elastic material properties of the waveguide, and we introduce '**:**' as a shorthand notation for a double index contraction.
Fundamental acoustic equation of (7) can be rewritten as:

$$\rho\, \partial_t^2 \mathrm{U}_i = \sum_{jkl} \partial_j c_{ijkl}\, \partial_k \mathrm{U}_l\,. \tag{9}$$

Here, ∂_j denotes the spatial derivative in the j-th spatial direction along j, where $j \in \{x, y, z\}$.

In a manner similar to the optical scenario, we now present a notation for the acoustic state vector$|\phi\rangle = \binom{\boldsymbol{T}}{\boldsymbol{V}}$, where $\boldsymbol{V} = \partial_t \boldsymbol{U}$ is the local velocity field. We proceed to approximate the acoustic state based on the eigenmodes of the (lossless, devoid of any external forces) acoustic waveguide [17]:

$$(\mathbb{D}^{ac} + iq\mathbb{P}^{ac})|\Phi\rangle = i\, \Omega\, \mathbb{E}^{ac}\, |\Phi\rangle, \tag{10}$$

Where

Table 1 Optical and acoustic properties of the waveguide materials [19]

Material	Relative permittivity	Photoelastic coefficients			Stiffness constants			Density
	ε_r	P_{11}	P_{12}	P_{44}	C_{11}[Pa]	C_{12}[Pa]	C_{44}[Pa]	ρ[kgm^{-3}]
Si	12.25	-0.09	0.017	-0.051	2.17×10^{11}	4.83×10^{10}	6.71×10^{10}	2329
SiO_2	2.25	0.121	0.27	-0.075	7.85×10^{10}	1.61×10^{10}	3.12×10^{10}	2201

$$\mathbb{E}^{ac} = \begin{pmatrix} \boldsymbol{s}: & 0 \\ 0 & \rho \end{pmatrix}, \tag{11.a}$$

$$\mathbb{P}^{ac} = \begin{pmatrix} 0 & -\hat{\boldsymbol{z}}\otimes_s \\ -\hat{\boldsymbol{z}}. & 0 \end{pmatrix}, \tag{11.b}$$

$$\mathbb{D}^{ac} = \begin{pmatrix} 0 & -\boldsymbol{\nabla}_{\perp,s} \\ -\boldsymbol{\nabla}_{\perp}. & 0 \end{pmatrix}. \tag{11.c}$$

Here, we define the symmetrized tensor product $\otimes_s$ by $\hat{\boldsymbol{z}}\otimes_s \boldsymbol{V} = (\hat{\boldsymbol{z}}\otimes \mathbf{V} + \mathbf{V}\otimes \hat{\boldsymbol{z}})/2$. The nonlinear optomechanical processes that dominate Brillouin scattering constitute inelastic scattering processes between two photons and one phonon. As a result, we will include only a single acoustic mode, leading to the following expansion:

$$|\phi(x,y,z,t)\rangle = b(z,t)\exp i(qz-\Omega t)\,|\Phi(x,y)\rangle + c.c. \tag{12}$$

2.3 Gain Calculation

In SBS, a three-wave interaction takes place, resulting in spatially stimulated optical gain. The geometry under consideration is that of a z-invariant waveguide, which can supp ort both optical and acoustic waveguide modes. For the guided opto-mechanical modes, the pump (p) and Stokes (s) waves, as well as the elastic wave, are taken to be of the form [18]:

$$\boldsymbol{E}_p(\boldsymbol{r},t) = a_p(z,t)\boldsymbol{e}_p(x,y)\exp i\left(k_p z-\omega_p t\right) + c.c. \tag{13}$$

$$\boldsymbol{E}_s(\boldsymbol{r},t) = a_s(z,t)\boldsymbol{e}_s(x,y)\exp i(k_s z-\omega_s t) + c.c. \tag{14}$$

$$\boldsymbol{U}(\boldsymbol{r},t) = b(z,t)\boldsymbol{u}(x,y)\,exp\,i(qz-\Omega t) + c.c. \tag{15}$$

where optical angular frequency and wave vector, ω_i and k_i $(i=p,s)$ and the acoustic frequency and wave vector, Ω and q, are related in the conventional manner concerning their propagation velocities. As a result of the conservation of energy and momentum, the subsequent relationships between frequency and wave vectors must be fulfilled: $\Omega = \omega_p - \omega_s$ and $q = k_p - k_s$.

Utilizing the slowly varying envelope approximation on the longitudinal aspect of the governing equations results in the subsequent coupled equations for the envelopes [18]:

$$\left(v_p\partial_z + \partial_t + \frac{v_p\alpha_p}{2}\right)a_p = -ig_0 a_s b, \tag{16}$$

$$\left(\pm v_s\partial_z + \partial_t + \frac{v_s\alpha_s}{2}\right)a_s = -ig_0{}^{*}a_p b^{*}, \tag{17}$$

$$\left(v_m\partial_z + \partial_t + (i\Delta_m + \frac{\gamma_m}{2})\right)B = -ig_0{}^{*}a_s{}^{*}a_p, \tag{18}$$

where $v_{p,s,m}$ represent the pump, Stokes, and mechanical group velocities, the upper and lower signs in the ± symbols in Eq. (16) account for either *forward* (upper sign) or *backward* (lower sign) SBS, $\alpha_{p,s}$ are the optical power attenuation coefficient, $\Delta_m = \Omega - \Omega_m$ is the frequency mismatch between the pump-Stokes beating and acoustic mode, $\gamma_m = \frac{\Omega_m}{Q_m}$ is the mechanical energy damping rate of a mode with quality factor Q_m. g_0 is the waveguide optomechanical

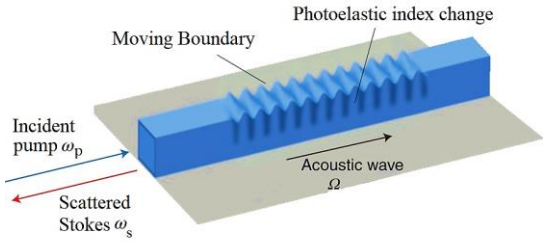

Fig. 2 Schematic of photoelastic and moving boundary effects.

coupling constant, which is calculated by integrating the interaction energy between the optical and mechanical modes over the waveguide's cross-sectional area, taking into account the radiation pressure and electrostriction interaction mechanisms.

The mechanical deformation influences the electromagnetic field in two distinct manners. Firstly, it alters the permittivity value, a phenomenon referred to as the *photoelastic* (PE) effect. Secondly, the displacement of material boundaries exerts work on the fields, an effect that lacks a widely recognized name, which we designate as *moving boundary* (MB) scattering (Fig. 2). In subwavelength waveguides, these two physical parameters are significant in the context of Brillouin gain. The first parameter is Q_{PE}, which can be articulated through a surface integral, whereas the second is Q_{MB}, which serves as a counteraction to radiation pressure [20]:

$$Q_{PE} = -\varepsilon_0 n^4 \boldsymbol{P}:\boldsymbol{S}\ \frac{\int dA\left(\boldsymbol{E}_p{}^{*}\cdot\boldsymbol{E}_s\right)}{\max(|\boldsymbol{u}|)\,N_p N_s}, \tag{19}$$

$$Q_{MB} = \frac{\int(\boldsymbol{u}^{*}\cdot\hat{\boldsymbol{n}})dr\ \left[\delta\varepsilon_{MB}\,\boldsymbol{E}^{*}{}_{p,\parallel}\cdot\boldsymbol{E}_{s,\parallel} - \delta\varepsilon_{MB}{}^{-1}\,\boldsymbol{D}^{*}{}_{p,\perp}\cdot\boldsymbol{D}_{s,\perp}\right]}{\max(|\boldsymbol{u}|)N_p N_s}. \tag{20}$$

In the above, $\boldsymbol{P}$ represents the fourth rank photoelastic tensor. The variable n signifies the material refractive index, and $\delta\varepsilon_{MB}$ is defined as $(\varepsilon_{core} - \varepsilon_{clad})$. Additionally, $\delta\varepsilon_{MB}{}^{-1}$ is expressed as $(\frac{1}{\varepsilon_{core}} - \frac{1}{\varepsilon_{clad}})$ in which $\varepsilon_{core} = \varepsilon_0 {n_1}^2$ and $\varepsilon_{clad} = \varepsilon_0 {n_2}^2$ refer to the permittivity of the waveguide's core and clad respectively. $\boldsymbol{u}\cdot\hat{\boldsymbol{n}}$ is the surface-normal component of the displacement vector $\boldsymbol{u}$ (the normal vector $\hat{\boldsymbol{n}}$ is directed from the core towards the clad); the fields $\boldsymbol{E}_{j,\parallel}$ and $\boldsymbol{D}_{j,\perp}$ are material interface tangential electric and normal displacement fields for the pump ($j = p$) or scattered ($j = s$) optical mode. The denominator in Eqs. (18),(19) represents the energy or power normalization integrals $N_i = (2\Re[\int(\boldsymbol{E}_i \times \boldsymbol{H}_i{}^{*})\cdot\hat{z}\,dA])^{1/2}$, with i being either p or s. Equation (18) is integrated over the entire transverse cross-section of the waveguide, while Equation (19) requires a line integral to be performed along the waveguide's boundaries. The SBS total gain of a particular combination of pump, Stokes and elastic modes is calculated as follows: [21]:

$$G_B = Q_m\ \frac{2\omega_p}{\bar{\mathrm{m}}_{eff}\ {\Omega_m}^2}|Q_{PE} + Q_{MB}|^2\,, \tag{21}$$

where Q_m is the mechanical energy quality factor, $\bar{\mathrm{m}}_{eff} = \int\frac{\rho|\boldsymbol{u}_m|^2}{max|\boldsymbol{u}_m|^2}\,dA$ is the effective linear mass density of a mechanical mode with displacement profile $\boldsymbol{u}_m$, ρ is the mass density.

3 Results and Discussion

We analyze the under-etched rectangular waveguide illustrated in Fig. 3. The silicon waveguide, which is partially suspended and aligned with a ⟨110⟩ axis, operates at a wavelength of 1550 nm and is supported by a silica pillar anchor with a width of *d*. Table 1 provides a summary of the optical and mechanical properties of silicon and silica (SiO_2). For simplicity, we neglect loss and dispersion in the dielectric parameters. The two-dimensional Finite Element Method (FEM) is employed to determine the optical and elastic modes of a waveguide. The simulation is conducted using COMSOL Multiphysics software, which employs the electromagnetic wave and structural mechanics modules to determine electric and acoustic field modes by solving the corresponding equations of motion outlined in the preceding sections.

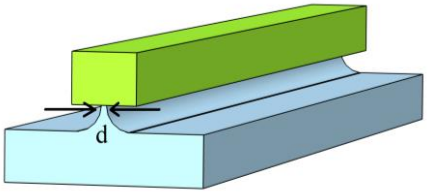

Fig. 3 The structure of the simulated partially suspended silicon waveguide on SiO_2. The cross-section dimensions measure 485 nm in width and 230 nm in height. The thickness of the pillar is represented by the variable *d*.

The distributions of electrical and acoustical fields within an SBS at specified frequencies are depicted in Fig. 4 and Fig. 5 for backward (BSBS) and forward scattering (FSBS), respectively. It is evident that in forward SBS, the electric field pattern exhibits a relatively smooth structure with a directional flow that aligns with the pump, signifying a gradual transfer of momentum. In backward SBS, the scattered electric field generates more pronounced standing-wave-like patterns, which is anticipated due to the interference between waves propagating forward and backward.

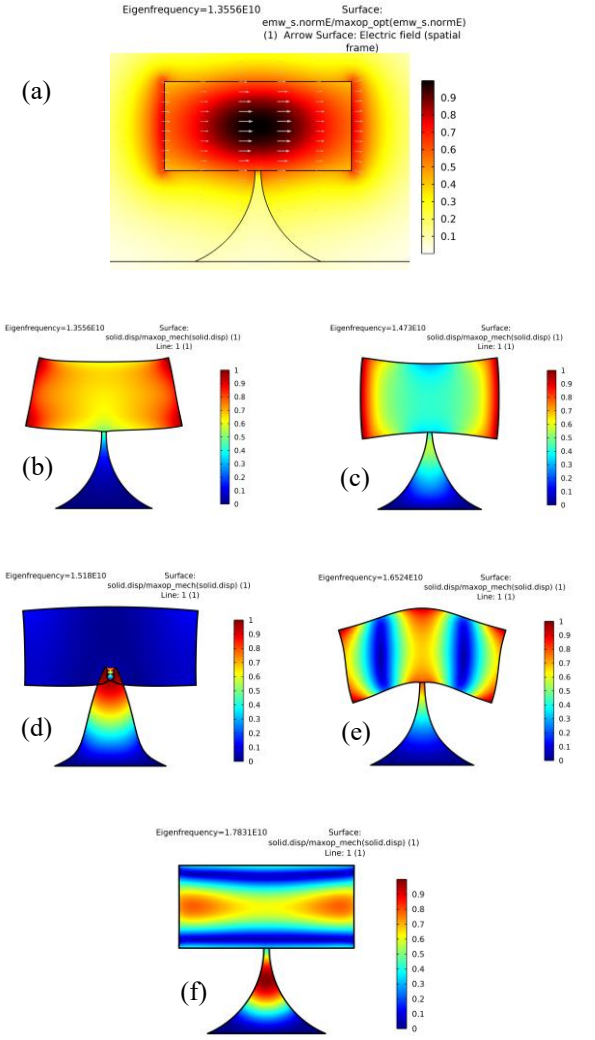

Fig. 4 Numerical simulation outcomes in backward SBS. (a) Normalized distribution of the electric field. The selective acoustic modes at their eigenfrequencies are shown in (b): 13.5 GHz, (c): 14.7 GHz, (d): 15.1 GHz, (e): 16.5 GHz, and (f): 17.8 GHz.

Concerning the acoustic mode shapes, in FSBS, the modes are predominantly transverse and flexural modes that interact with the optical field. Mode (e) at 12 GHz exhibits a pronounced shear-like displacement profile. Conversely, in BSBS, the acoustic modes are mainly longitudinal and hybrid acoustic modes (both axial and radial) at elevated frequencies. Mode (e) at 16.5 GHz exhibits significant field overlap with the optical mode, thereby enhancing the SBS gain. FSBS acoustic modes seem to be advantageous in the lower GHz range. Phonons engage over extended distances as a result of co-propagation. In BSBS, the high acoustic confinement and pronounced modal overlap at elevated GHz frequencies enhance phase matching and coupling strength.

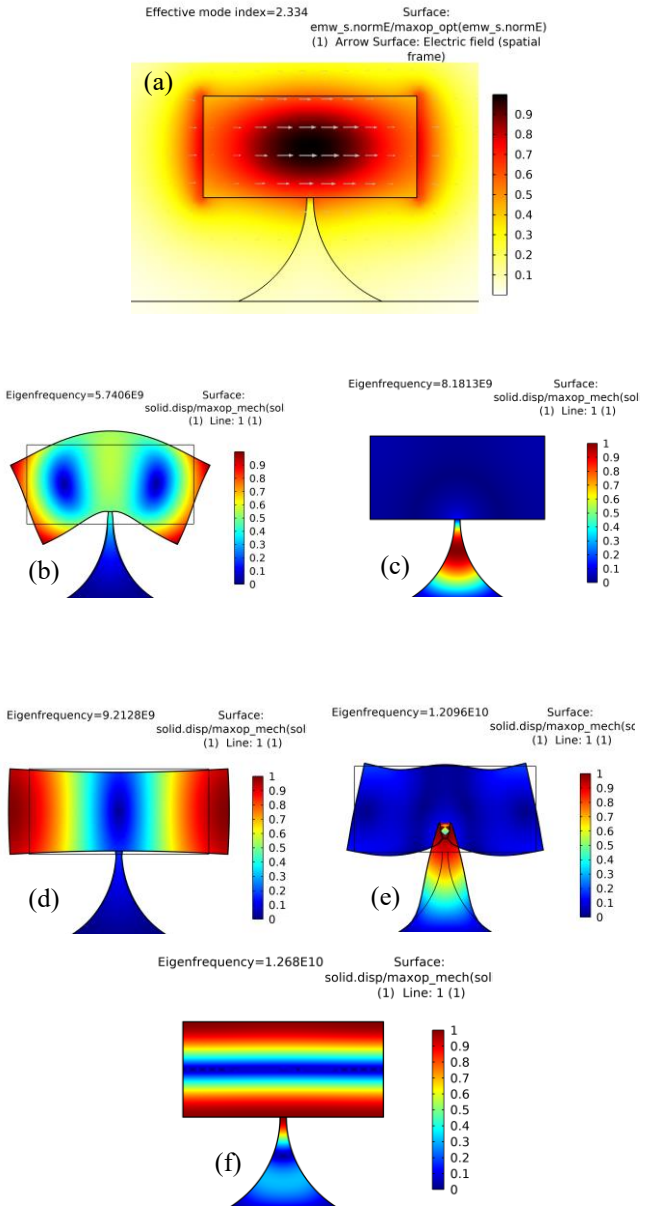

Fig. 5 Numerical simulation outcomes in forward SBS. (a) Normalized distribution of the electric field. The selective acoustic modes at their eigen-frequencies are shown in (b): 5.7 GHz, (c): 8.1 GHz, (d): 9.2 GHz, (e): 12 GHz, and (f): 12.6 GHz.

To conduct a thorough investigation, a gain analysis of BSBS is also performed. The outcomes of the gain concerning variations in frequency for photoelastic and moving boundary effects, along with the impact of the width of the pillar anchor, are depicted in Fig. 6. Sharp peaks in Fig. 6(a) indicate strong phase-matched coupling between the optical and acoustic modes at those frequencies. The PE effect dominates the total gain at two clear resonances: 14.73 GHz and 17.83 GHz. At both peaks, PE contributes the majority

of the gain, indicating these are bulk strain-driven interactions. The MB effect arises from modulations of the waveguide boundaries and exhibits a secondary contribution at frequencies similar to those of the PE peaks, but is significantly smaller (~20% or less). The MB effect also slightly contributes near 15.18 GHz, where PE is minimal, suggesting a surface-localized acoustic mode. These peaks in gain correlate well with the optically active acoustic eigenmodes identified in the backward SBS configuration, indicating efficient phase-matching and spatial mode overlap. Figure 6 (b) reveals a clear trend: with an increase in pillar width from 10 nm to 40 nm, the total Brillouin gain/Q_m shows a consistent decrease from 5.48 to 0.68. Increasing the anchor width causes acoustic waves to leak into the substrate, reducing the overlap between acoustic and optical modes. The suspension must be thin enough to minimize acoustic losses but robust enough for mechanical stability. Although the main effect is acoustic, the anchor geometry can indirectly affect optical modes by altering the field distribution, which also influences mode overlap and gain. The waveguide's cross-sectional dimensions are also key factors influencing its performance. Optimized dimensions enhance the confinement of optical and acoustic modes, improving their spatial overlap and Brillouin gain [22].

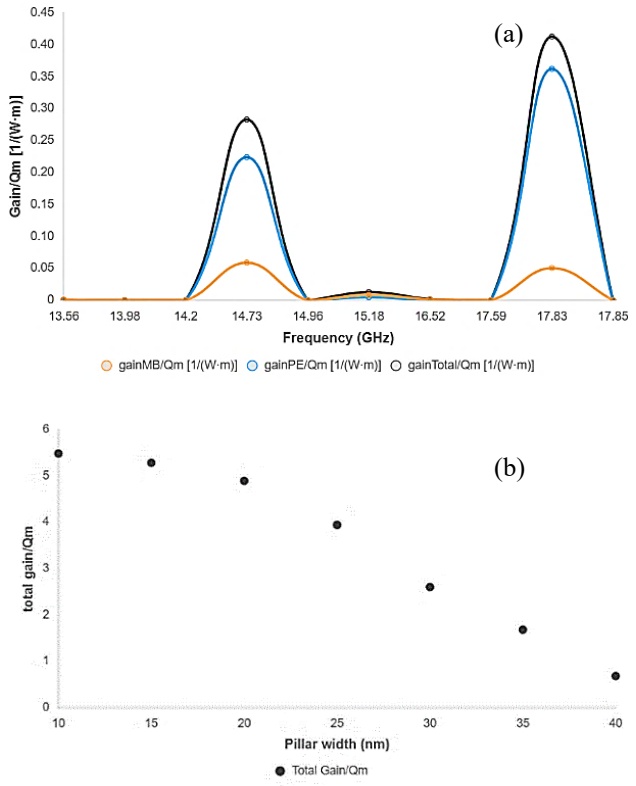

Fig. 6 (a) Total, MB, and PE Brillouin gain as a function of frequency for backward scattering (d=40 nm). (b) Total Brillouin gain as a function of pillar width.

4 Conclusion

We presented a comprehensive numerical investigation of forward and backward stimulated Brillouin scattering (SBS) in a partially suspended, z-invariant silicon rectangular waveguide. Using finite element method, we analyzed the electric field distributions and selectively coupled acoustic eigenmodes over a wide frequency range for both SBS configurations. Numerical results reveal stronger vertical and lateral confinement of the acoustic modes in the range of 13.5–17.8 GHz., further supported by gain analysis. The frequency-dependent SBS gain reveals that the photoelastic PE effect is the dominant coupling mechanism, particularly at the resonant frequencies. The MB effect contributes modestly, adding marginal gain where surface acoustic displacement is significant. The suspended design significantly reduces substrate-induced losses, facilitating effective phonon-photon coupling, which is essential for applications like on-chip optical signal processing and sensing. Our research underscores the necessity of optimizing pillar width in suspended waveguides to enhance Brillouin scattering efficiency, thereby offering a route for the development of advanced photonic devices with superior performance in integrated optoelectronic systems. Future investigations could examine the effects of material variations and structural changes to improve gain at larger widths. In summary, the findings reveal that the partially suspended waveguide configuration not only provides strong acoustic confinement but also allows for customized modal coupling across a broad frequency range.

References

1. R. W. Boyd, *Nonlinear Optics*, 3rd ed. Academic Press, SanDiego, CA, (2008)
2. L. Brillouin, *Ann. Phys.* **17**, (1922)
3. R. Y. Chiao, C. H. Townes, B. P. Stoicheff, *Phys. Rev. Lett.* **12**, (1964)
4. Z. Bai, H. Yuan, Z. Liu, P. Xu, Q. Gao, R.J. Williams, O. Kitzler, R. P. Mildren, Y. Wang, Z. Lu, *Opt. Mater.* **75**, (2018)
5. N. T. Otterstrom, R. O. Behunin, E. A. Kittlaus, Z. Wang, P. T. Rakich, *Science* **360**, (2018)
6. S. Gundavarapu, G. M. Brodnik, M. Puckett, T. Huffman, D. Bose, R. Behunin, J. Wu, T. Qiu, C. Pinho, N. Chauhan, J. Nohava, P. T. Rakich, K. D. Nelson, M. Salit, D. J. Blumenthal, *Nat. Photonics* **13**, (2019)
7. A. Choudhary, I. Aryanfar, S. Shahnia, B. Morrison, K. Vu, S. Madden, B. Luther-Davies, D. Marpaung, B. J. Eggleton, *Opt. Lett.* **41**, (2016)

8. D. Marpaung, B. Morrison, M. Pagani, R. Pant, D.-Y. Choi, B. Luther-Davies, S. J. Madden, B. J. Eggleton, *Optica* **2**, (2015)
9. C. G. Poulton, R. Pant, A. Byrnes, S. Fan, M. Steel, B. J. Eggleton, Opt. Express **20**, (2012)
10. E. A. Kittlaus, N. T. Otterstrom, P. Kharel, S. Gertler, P. T. Rakich, *Nat. Photonics* **12**, (2018)
11. M. Merklein, B. Stiller, K. Vu, S. J. Madden, B. J. Eggleton, *Nat. Commun*. **8**, (2017)
12. M. Merklein, B. Stiller, B.J. Eggleton, *J. Opt.* **20**, (2018)
13. J. Li, M.G. Suh, K. Vahala, *Optica* **4**, (2017)
14. M. Bagheri, M. Poot, L. Fan, F. Marquardt, H. X. Tang, *Phys. Rev. Lett.* **111**, (2013)
15. S. Hong, R. Riedinger, I. Marinkovi´c, A. Wallucks, S. G. Hofer, R. A. Norte, M. Aspelmeyer, S. Gröblacher, *Science* **358**, (2017)
16. R. Van Laer, B. Kuyken, D. Van Thourhout, R. Baets, *Nat. Photonics* **9**, (2015)
17. C. Wolff, M. J. A. Smith, B. Stiller, C. G. Poulton, *J. Opt. Soc. Am. B* **38**, (2021)
18. G. Wiederhecker, P. Dainese, T.P.M. Alegre, *APL Photon.* **4**, (2019)
19. S. R. Mirnaziry, C. Wolff, M. J. Steel, B. J. Eggleton, C. G. Poulton, *Opt. Express* **24**, (2016)
20. C. Wolff, M. Steel, B. Eggleton, C. Poulton, *Phys. Rev. A,* **92**, (2015)
21. J.E. Sipe, M.J.A. Steel, *New J. Phys.* **18**, (2016)
22. K Ramadhan et al, J. Phys.: Conf. Ser. **2866**, (2024)